Available online at www.sciencedirect.com

SciVerse ScienceDirect

Acta Materialia 61 (2013) 2725–2733

Acta MATERIALIA

www.elsevier.com/locate/actamat

Misfit accommodation in oxide thin film heterostructures ☆

S.J. Pennycook [a,b,*], H. Zhou [c], M.F. Chisholm [a], A.Y. Borisevich [a], M. Varela [a], J. Gazquez [d], T.J. Pennycook [e], J. Narayan [c]

[a] Materials Science and Technology Division, Oak Ridge National Laboratory, Oak Ridge, TN 37831, USA
[b] Department of Materials Science and Engineering, University of Tennessee, Knoxville, TN 37996, USA
[c] Department of Materials Science and Engineering, North Carolina State University, Raleigh, NC 27695, USA
[d] Departamento de Física Aplicada III, Universidad Complutense de Madrid, Madrid 28040, Spain
[e] SuperSTEM, Daresbury, UK

Available online 7 January 2013

Abstract

Complex oxides are of intense interest due to their diverse properties, such as colossal magnetoresistance and superconductivity. Their complexity arises not only from the number of constituent elements, but also from their tolerance of non-stoichiometry and the structural complexity of these perovskite-based materials, e.g. the distortions and rotations of the oxygen octahedra surrounding the B-site cation. For these reasons, misfit accommodation in these materials is far more complex than in simpler materials, and can involve several different mechanisms simultaneously. In some cases, interfaces can be free from any misfit dislocations, lattice mismatch being accommodated via incorporation of oxygen vacancies, which take an ordered periodic arrangement. Interfaces may also present a perturbation to the octahedral rotations that can dramatically affect properties, not just close to the interface but through the entire film. In oxygen ion conducting materials, the oxygen sublattice may even melt in some situations.
© 2012 Acta Materialia Inc. Published by Elsevier Ltd. All rights reserved.

Keywords: Thin films; Defects; Dislocations; Misfit relaxation

1. Introduction

The explosion of interest in the field of oxides, especially the so-called complex oxides, is due to the wealth of new phenomena they exhibit, such as colossal ionic conductivity and magnetoresistance, and the emergence of new superconducting, magnetic and electronic properties [1–3]. Even more exotic phenomena have been found at interfaces in oxide heterostuctures. For example, the seemingly simple interface between the two insulators $LaAlO_3$ and $SrTiO_3$ can be metallic [4], ferromagnetic or superconducting [2,5]. Even more degrees of freedom exist in complex oxide heterostructures, where octahedral distortions and associated changes in orbital occupation can take place, e.g. the orbital reconstruction observed in superconducting/ferromagnetic cuprate/manganite heterostructures [1,6].

Misfit accommodation can be similarly complex. Generally, stress in thin films is relaxed by dislocations, which nucleate at free surface steps and glide to the interface. Thus, kinetics of dislocation nucleation and propagation play a critical role in thin film relaxation processes. Surface steps play a critical role in dislocation nucleation, and lattice frictional stress determines propagation [7,8]. Only when a component of the film stress, known as the critical resolved shear stress, acting on dislocations in the glide plane, exceeds the yield stress/lattice frictional stress will the dislocation propagate. The critical resolved stress is given by $\sigma_f \cos\varphi\cos\lambda$ (Schmid factor), where σ_f is the planar stress, φ is the angle between the stress direction and the glide direction, and λ is the angle between the stress

☆ This article was presented at the symposium held in honor of Professor Jagdish Narayan, the recipient of the Acta Materialia Gold Medal Award.

* Corresponding author at: Materials Science and Technology Division, Oak Ridge National Laboratory, Oak Ridge, TN 37831, USA.
E-mail address: Pennycooksj@ornl.gov (S.J. Pennycook).

1359-6454/$36.00 © 2012 Acta Materialia Inc. Published by Elsevier Ltd. All rights reserved.
http://dx.doi.org/10.1016/j.actamat.2012.09.069

direction and the glide plane normal. For certain film/substrate orientations, the Schmid factors may be too small or zero for available slip systems. This would prevent the generation of misfit dislocations. Under these conditions, films having large misfits can grow without dislocations up to a certain thickness without a fracture/crack. In complex oxides there are many additional possible mechanisms. Dislocation cores can be non-stoichiometric, and the entire misfit may be accommodated by alternative means, for example through the introduction of oxygen vacancies, which can lead to lattice parameter changes [9]. In addition, mismatch can occur not only in the lattice parameter but, in the case of perovskites, also in the octahedral tilt network, again radically influencing the film properties. A detailed atomic resolution characterization of the interface atomic and electronic structure, ideally coupled to electronic structure calculations, is critical to understand and control the structure–property relations in these materials.

Scanning transmission electron microscopy (STEM) is ideally suited to a study of this nature as it is able to provide multiple signals simultaneously at atomic resolution [10], specifically, the Z-contrast image (through a high- or medium-angle annular detector [11–13]), a bright-field (phase-contrast) image [14] and electron energy loss spectroscopic (EELS) images reflecting the elemental composition and electronic structure [15,16]. With the successful correction of objective lens aberrations, the spatial resolution, precision and sensitivity of these measurements have been dramatically improved, as described in a number of recent reviews [17,18]. However, particularly in the case of dislocation cores, it must be remembered that not all contrast is Z-contrast [19–21]. The high strain fields of the dislocation cores can disturb the crystal orientation, either directly or through surface relaxations, leading to image contrast. Depending on the detector angle, such contrast can be bright or dark; indeed, it is possible to determine the nature of the Burgers vectors from the symmetry of the contrast [22–24]. Similar contrast effects will be present in EELS signals, so that quantitative interpretation of composition maps at dislocation cores is also difficult. In addition, although it is generally assumed that the fine structure shown by EELS can be interpreted in terms of oxidation states – particularly useful for the transition metal L edges – the influence of diffraction/channeling conditions on such signals has yet to be rigorously established in the case of atomic resolution.

Here, we use these techniques to illustrate the rich variety of misfit accommodation processes utilized by oxide thin films and heterostructures. We show an example of domain matching epitaxy [25], with the formation of misfit dislocations and additional strain relief through dislocation core segregation. We then show examples of the formation of metastable intermediate phases at interfaces, and of misfit accommodation via vacancy arrays, which avoids the formation of misfit dislocations entirely. We then show how, in perovskite films, the additional order parameter represented by the octahedral tilt network provides a new mechanism for misfit accommodation that has a major influence on interfacial properties. Finally, we show an extreme example where the O ion sublattice actually disorders, or melts, with a colossal increase in ionic conductivity.

2. Dislocation core structures at a non-polar ZnO/Al_2O_3 interface

Non-polar ZnO and GaN films are of interest for light emission applications since they avoid the strong piezoelectric polarization fields which tend to separate electrons and holes, thus reducing the internal quantum efficiency [26–29]. This system is actually a classic example of so-called domain matching epitaxy [25] in which a high mismatch can be fully relaxed during film growth by matching different integer numbers of planes in the two materials. Choosing the *r*-plane of sapphire ($(1\,\bar{1}\,0\,2)$ Al_2O_3) as a substrate, ZnO grows epitaxially with its *a*-plane ($(1\,1\,\bar{2}\,0)$ ZnO) parallel to the sapphire *r*-plane, with in-plane orientations of $[0\,1\,\bar{1}\,0]$ ZnO // $[2\,\bar{1}\,\bar{1}\,0]$ Al_2O_3 and $[0\,0\,0\,1]$ ZnO // $[\bar{1}\,1\,0\,1]$ Al_2O_3 [30–32]. The lattice mismatch in these two directions is quite different – 18.3% for the former direction but only 1.5% for the latter direction – and, perhaps surprisingly, it is the high mismatch that is relaxed completely during the growth process. The explanation is that in the high mismatch direction it is simple to nucleate dislocations during film growth because the critical thickness is below one monolayer. Such relaxation has been commonly

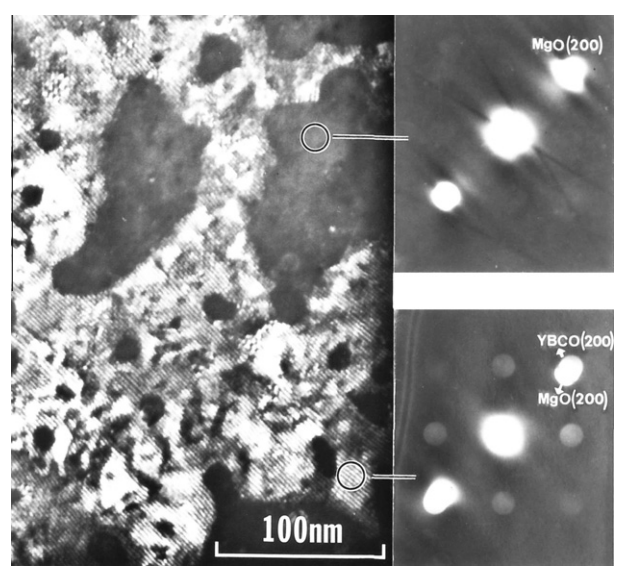

Fig. 1. Dark-field plan-view TEM image from a three unit cell $YBa_2Cu_3O_{7-x}$ (YBCO) film deposited on MgO taken with a YBCO {100} reflection, which is forbidden in MgO, with microdiffraction patterns from the bare substrate (top) and a portion of the YBCO film (bottom). The dark regions in the image represent bare substrate, and the intensities from the YBCO film are quantized, indicating single, double and triple unit cell regions. Moiré fringes indicate that relaxation has occurred even in the single unit cell regions of the film. The misfit is 9.3 and 7.6% along the *a* and *b* directions of the YBCO, respectively. Reproduced from Ref. [34].

observed in high temperature superconductor films, for example [33–35] (see Fig. 1). However, in the present case, the mismatch is much more highly anisotropic, and in the low mismatch direction the critical thickness is much higher, so relaxation must proceed via the nucleation of dislocation loops at the surface of the growing film followed by glide to the interface [36]. This process has a high activation energy and typically results in incomplete strain relaxation – as, indeed, in the present case [32].

In the high mismatch direction, however, the strain is almost fully relaxed [25,32]. Cross-section Z-contrast images taken with a VG Microscopes HB 603U scanning transmission electron microscope equipped with a Nion aberration corrector operating at 300 kV accelerating voltage are shown in Fig. 2. They reveal an array of misfit dislocations (arrowed) consistent with the 18.3% lattice mismatch [37]. The higher magnification view in Fig. 2b shows the bright hexagonal arrangement of the ZnO columns aligned with the Al columns of the Al_2O_3. The O columns in the Al_2O_3 are just visible, forming a sequence of "cross"- and "ring"-shaped units along the interface plane. There are hence two possible alignments with the ZnO lattice, as indicated in Fig. 2c. Configuration A is expected to have lower energy than configuration B as the bond lengths and angles are closer to the bulk values; indeed, this is the configuration observed in between the dislocation cores. Fig. 2d shows how configuration B would arise halfway between two of the preferred configurations, which is where the dislocation cores are located, thereby avoiding this higher energy configuration.

A further means to reduce the strain field surrounding the dislocation core is observed in some cores but not all. The dislocation on the far right-hand side of Fig. 2 shows a bright region in the center of the core. Fig. 3 shows a higher magnification comparison of two cores with and without the bright columns, along with schematic structures showing the reduced strain surrounding the core containing the bright columns. EELS indicates that the columns contain Zn. This would appear surprising, since Zn has a larger ionic radius than Al and segregates to the compressive side of the dislocation core, which would seem to increase the strain. However, the modified core structure with the Zn seems to be more compact, i.e. the strained/distorted ZnO region is confined to a smaller region with respect to that in dislocations with the unmodified core structure, suggesting that the modification leads to a certain degree of strain relief in ZnO. We speculate that this is attributable to the lower valence of Zn (2+, with respect to the 3+ of Al). A lower valence means that fewer oxygen ions are required for bonding and, as a result, the Zn-modified core reduces the strain. O deficiency has been observed previously in dislocation cores in oxides [38,39].

3. Formation of interfacial transition layers in VO_2/Al_2O_3 heterostructures

Interfacial transition phases that are not stable or even do not exist in bulk have been observed in a variety of systems, including γ-Fe_2O_3 on MgO (0 0 1) [40], a Co_2O_3 corundum phase on α-Al_2O_3 (0 0 0 1) [41] and hexagonal $DyMnO_3$ on $ZrO_2(Y_2O_3)$ (1 1 1) [42]. We show here two examples from epitaxial VO_2 thin films grown on an Al_2O_3 substrate, in the first case directly and in the second case with an intermediate NiO layer. Because of its near-room-temperature (68 °C) semiconductor–metal transition, VO_2 is of major interest for sensing and switching applications in microelectronics [43]. Because of its monoclinic structure, matching to a suitable substrate can be difficult;

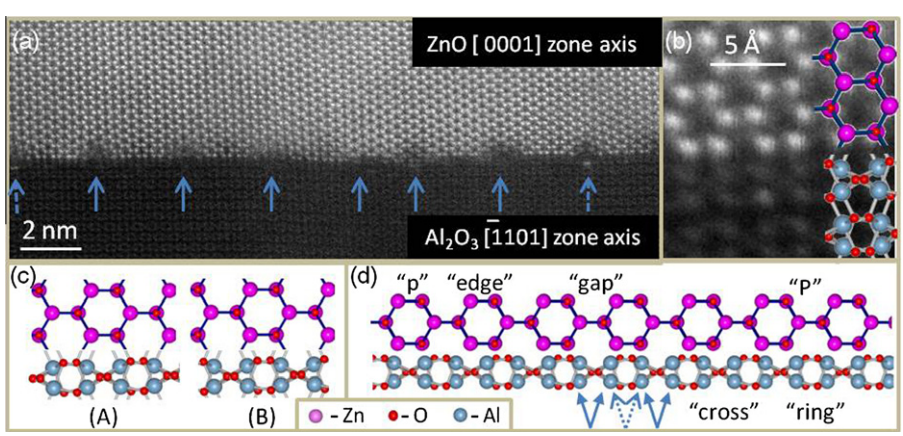

Fig. 2. (a) STEM-Z contrast image of the (1 1 $\bar{2}$ 0) ZnO/(1 $\bar{1}$ 0 2) Al_2O_3 interface along the ZnO[0 0 0 1]/Al_2O_3 [$\bar{1}$ 1 0 1] zone axis. Misfit dislocations, indicated by arrows, are characterized by an extended strained region (seen as dark in the image) on the ZnO side of the interface. (b) Higher magnification Z-contrast image of the interface between two misfit dislocation cores showing the preferred interfacial bonding configuration. (c) Schematic illustration of the two possible interfacial bonding configurations. Configuration (A), where the ZnO "hexagon edge" is bonded with an Al_2O_3 "cross", is expected to be energetically more favorable than configuration (B), where the ZnO "hexagon edge" is bonded with the Al_2O_3 "ring", owing to the reduced bond distortion required. (d) Schematic diagram of the interface drawn in proportion to the bulk lattice constants of the two materials, with both ends in the preferred bonding configuration (ZnO "hexagon edge"–Al_2O_3 "cross" or ZnO "gap"–Al_2O_3 "ring", indicated by "P"). Pairs of arrows point to the possible locations of the dislocation line, i.e. two extra Al_2O_3 planes. Dashed arrows point to the location where broken ZnO bonds would be required, which is where the dislocation cores locate. Reproduced from Ref. [37].

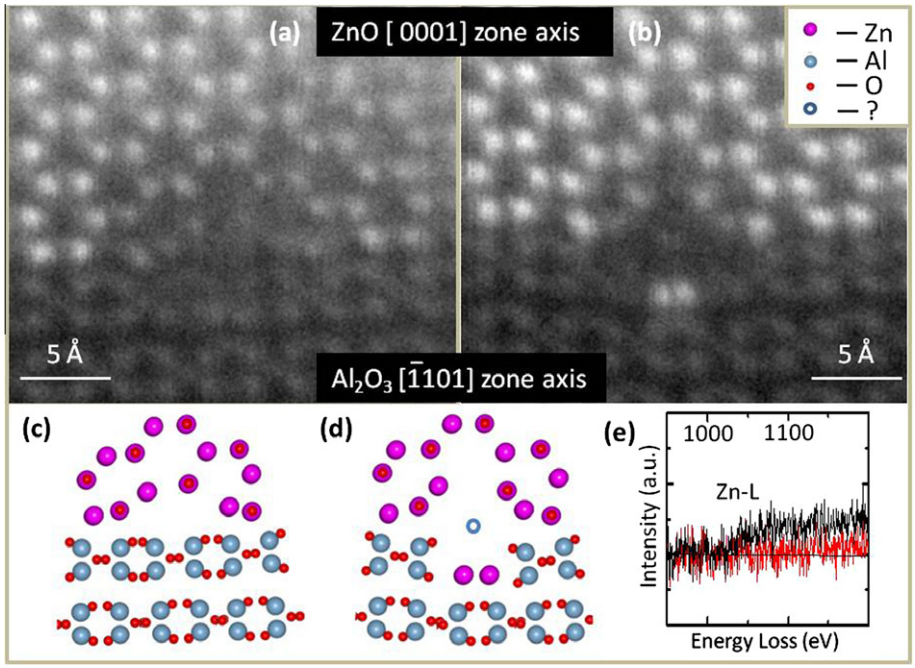

Fig. 3. Atomic resolution Z-contrast image of the most frequently observed misfit dislocation core structure (a), along with its deduced model (c). The Burgers vector of the dislocation is determined to be $1/3\langle 2\,\bar{1}\,\bar{1}\,0\rangle$ Al_2O_3. Atomic resolution Z-contrast image of a modified misfit dislocation core structure involving replacing Al atoms in the core region by Zn (b) and its deduced model (d). The tensile strain in the core region is reduced compared with that in the unmodified core, as deduced from the reduced extent of strain contrast (columns with reduced intensity) seen in the image. An EELS spectrum acquired on the bright columns, where Zn replaces Al at the Al_2O_3 side of the dislocation core, is shown in black, and one acquired outside the core region is shown in red (e). Though noisy, a Zn L edge is clearly present on the former. Reproduced from Ref. [37]. (For interpretation of the references to colour in this figure legend, the reader is referred to the web version of this article.)

however, V can take a large variety of oxidation states, and consequently oxides exist in many different stoichiometries, all based on octahedral coordination. Some of these phases show significant structural similarity to common substrates, as shown in Fig. 4. It is observed that in many cases VO_2 initially takes on the crystal structure of the substrate to avoid such mismatch, either preserving the stoichiometry of VO_2 or accommodating cation vacancies to better match the substrate crystal structure.

An example for the case of epitaxial VO_2 films grown on *c*-cut sapphire substrates, $(0\,0\,0\,1)$ Al_2O_3, is shown in Fig. 5, viewed along the Al_2O_3 $[2\,\bar{1}\,\bar{1}\,0]$ zone axis [44]. In this direc-

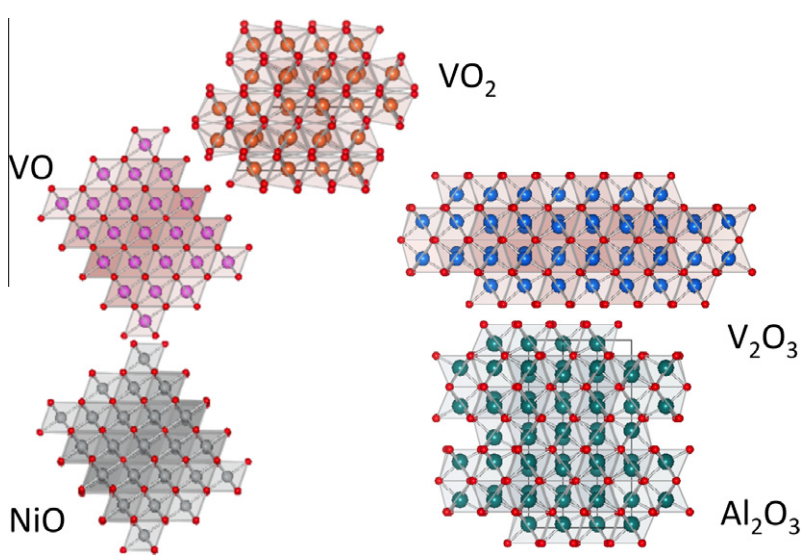

Fig. 4. Octahedra in various V oxides, NiO and Al_2O_3, with O shown as red spheres. (For interpretation of the references to colour in this figure legend, the reader is referred to the web version of this article.)

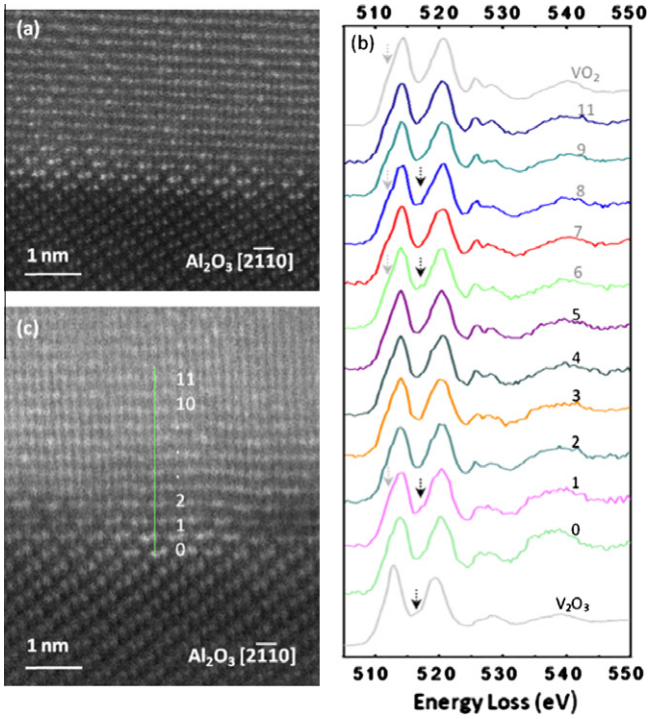

Fig. 5. (a) An ADF image of the interface along the Al_2O_3 [2 $\bar{1}$ $\bar{1}$ 0] zone axis. (b) A series of EEL spectra acquired along the direction perpendicular to the interface, labeled in order from "0" to "11", with "0" acquired at the "V_2O_3"-like interface region and "11" acquired inside the film. The green line in (c) roughly marks the region where the series of spectra was acquired. EELS from VO_2 (top) and V_2O_3 (bottom) are also included in (b) for comparison. Grey and dark arrows in (b) indicate the V^{4+} and V^{3+} signatures, respectively. Reproduced from Ref. [44]. (For interpretation of the references to colour in this figure legend, the reader is referred to the web version of this article.)

tion the Al columns form closely spaced pairs (dumbbells) that are aligned at an angle to the interface. The vanadium oxide shows bright Z-contrast due to the presence of the V; however, a few monolayers near the interface clearly continue the structure of the Al_2O_3, suggesting that it might actually be V_2O_3, with the heavier V atoms in the Al atom positions. In an attempt to confirm this, EELS data were acquired across the interface, as shown in Fig. 5b, with reference spectra from VO_2 and V_2O_3 for comparison. It is immediately clear that the V $L_{2,3}$ ratio does not change appreciably across the interfacial transition phase, neither is the expected chemical shift observed, indicating that, despite the V_2O_3 structure, a V^{4+} oxidation state is maintained as in VO_2. However, the distortion into a V_2O_3 structure manifests itself through the appearance of a number of features on the O K edge that are present in stoichiometric V_2O_3. This structure and the V^{4+} charge state can be explained by the creation of cation vacancies in this layer.

A much wider interfacial transition zone is seen at the VO_2/NiO interface, a heterostructure grown on *c*-cut single-crystal Al_2O_3 (0 0 0 1). Based on the previous discussion, we might anticipate VO to form, given that VO and NiO both have the rocksalt structure (see Fig. 4); furthermore, the transition zone might be wider, since the mismatch is only ~2% between stoichiometric VO and NiO compared with ~4% between V_2O_3 and Al_2O_3. Fig. 6a shows a high-resolution Z-contrast image of the VO_2/NiO interface viewed down an Al_2O_3 [0 1 $\bar{1}$ 0] crystal direction. The bright columns on the left side of the image are V columns, with the configuration expected when viewed down the VO_2 [1 0 0] direction. The even brighter columns on the right side of the image are Ni columns, with the configuration expected when viewed from the NiO [1 1 0] direction. The O columns are barely visible next to the bright V and Ni columns in this image. This is in agreement with the orientation relationship determined by X-ray diffraction, i.e. VO_2 (0 2 0) // NiO (1 1 1) // Al_2O_3 (0 0 0 1), with in-plane VO_2 [1 0 0] // NiO [1 1 0] // Al_2O_3 [0 1 $\bar{1}$ 0] [45]. In the center of the image an interfacial transition zone is clearly seen, where the atomic configuration seems to resemble that of NiO, but with a reduced intensity.

Fig. 6b shows EELS spectra taken from the numbered regions in the image. This time the fine structure of V in the transition zone (2 and 3) shows both a change in $L_{2,3}$ ratio and a chemical shift with respect to the VO_2 film, indicating a reduced stoichiometry (see the reference spectra in the inset). The O K edge structure also shows changes consistent with a reduced V oxidation state [46]. Thus the interfacial phase appears to be a vanadium oxide near the VO_2 with the structure of NiO but a reduced valence, which is presumably stabilized by V vacancies. The intensity of the columns increases towards the substrate, indicating mixed V/NiO. This is another example where the structure and valence states are affected by the presence of defects.

4. Formation of interfacial transition layers in perovskite-based heterostructures via octahedral rotations

With the successful correction of microscope lens aberrations, not only has the resolution improved, allowing the imaging of oxygen columns in perovskites [47,48], but also the precision with which atomic columns can be located has dramatically improved. It is now possible to locate even the light columns to picometer level precision, allowing the direct measurement of octahedral rotations from real space images [14,49,50]. Even when the film is almost lattice matched to the underlying layer, if the octahedral tilt system differs in the two materials, one will influence the other. An example is the case of an ultrathin film of $BiFeO_3$ (BFO) on $La_{0.7}Sr_{0.3}MnO_3$ (LSMO), as shown in Fig. 7. The Z-contrast image allows the *c*-axis lattice parameter to be determined with high accuracy, revealing an expanded *c* lattice parameter in the last four unit cells of the BFO. The reason for this expansion is revealed by analyzing the oxygen atom positions seen in the bright-field image, to determine the rotations of the oxygen octahedra. Since the LSMO has negligible octahedral rotations, the epitaxial BFO is constrained to match the tilts of the

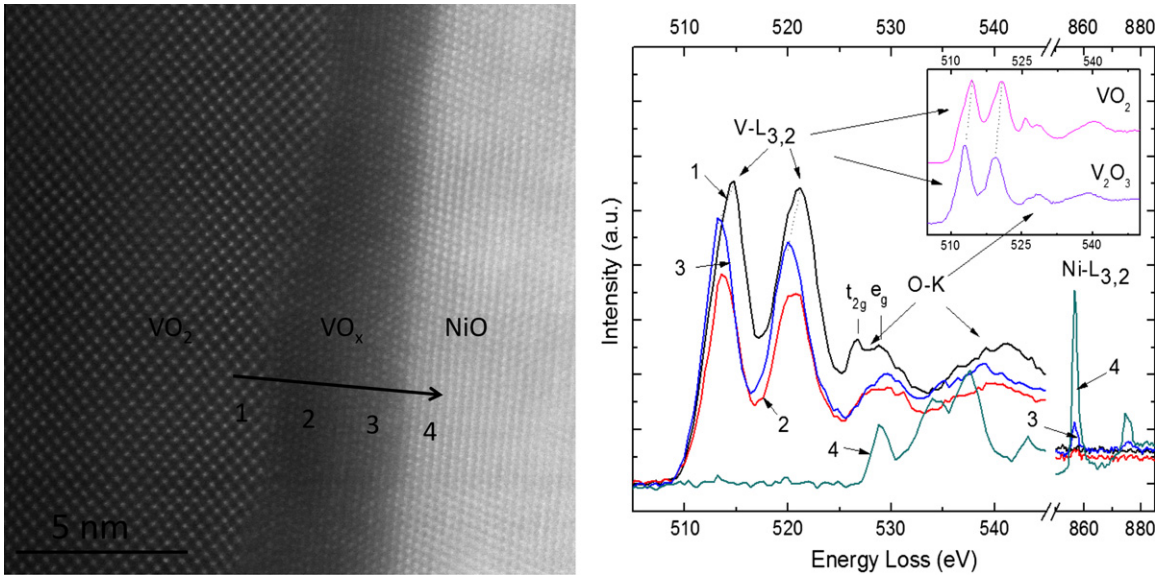

Fig. 6. (a) Z-contrast image of the NiO/VO_x/VO_2 heterostructure showing how the VO_x transition zone continues the structure of NiO. (b) EEL spectra from regions 1–4 compared to reference spectra (inset). The VO_x region shows the fine structure of V_2O_3 and a chemical shift with respect to the VO_2 edge. The O K edge is also similar to that of V_2O_3. The right-hand side shows the Ni $L_{2,3}$ edge from regions 2 and 3.

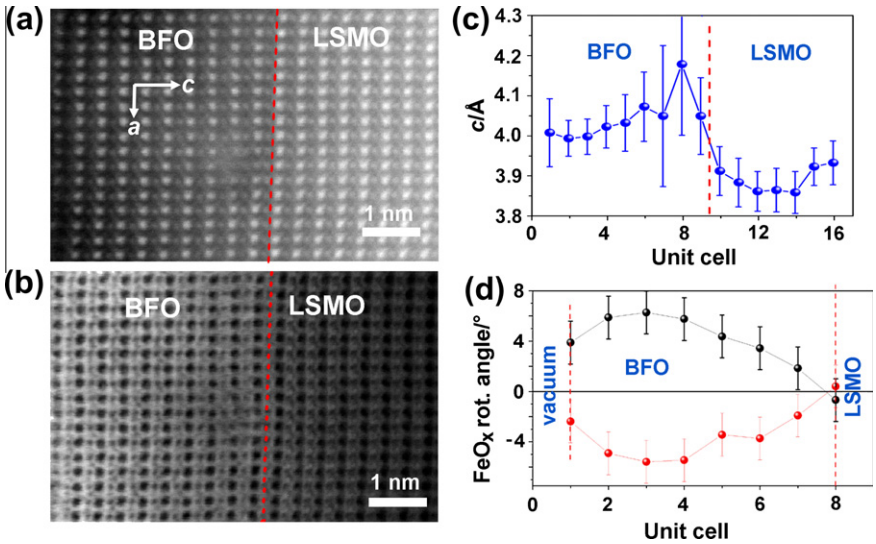

Fig. 7. Lattice parameters and octahedral tilts from combined (a) Z-contrast STEM and (b) simultaneously acquired bright-field STEM images of a $SrTiO_3$/5 nm $La_{0.7}Sr_{0.3}MnO_3$/3.2 nm $BiFeO_3$ (BFO) ultrathin film. (c) Profile of *c* lattice parameter across the interface calculated from (a). (d) Profile of FeO_x octahedral tilt angles in BFO calculated from (a) and (b). Note that lattice parameter enhancement at the interface in (c) coincides with a region of suppressed octahedral tilts in (d). Adapted from Ref. [14].

LSMO near the interface. This enforced tilt suppression leads to altered electronic properties, the signature of which can be seen in low-loss EELS [14].

The competing symmetry due to differing octahedral tilt systems leads to an interfacial layer with distortion modes that do not exist in either bulk material, and therefore creates new interface properties driven by symmetry alone. Depending on the resistance of the octahedra to deformation, the interface layer can be as small as one unit cell or can extend deep into the thin film [51–53].

5. Relaxation via ordered vacancy arrays

Many O ion-conducting perovskites can accommodate high concentrations of vacancies, which tend to order, thereby minimizing elastic stresses. The prototypical structure of this type is Brownmillerite, in which 1/6 of the O has been removed. It forms ordered vacancy chains in every other B site plane, i.e. alternating BO_2 and BO planes, with an overall stoichiometry of $ABO_{2.5}$. In fact, a wide range of vacancy concentrations can be accommo-

dated, and it is well established that the lattice parameter changes linearly with the vacancy concentration [9]. Consequently, it should not be too surprising that in these materials misfit strain can be efficiently relaxed through the incorporation of vacancies, hence avoiding the need for misfit dislocations. The resulting vacancy superstructure is readily visualized in a Z-contrast image because the vacancy-containing planes expand, leading to reduced image intensity [54–56]. The ordered vacancy arrays tend to form a domain structure, as shown in Fig. 8 for the case of a $La_{0.5}Sr_{0.5}CoO_{3-\delta}$ (LSCO) thin film [57].

Nanopockets in these films with especially high O deficiency were found to exhibit a superlattice not only in O concentration but also of Co atom spin, evident from the fact that the Co $L_{2,3}$ ratio was unchanged from dark to bright stripes but the O K edge fine structure did change, consistent with a change in spin state [58].

6. Oxygen sublattice melting in strained Y_2O_3-stabilized ZrO_2

An even more dramatic response of the O sublattice to strain is found in the case of strained Y_2O_3-stabilized ZrO_2 (YSZ). With $SrTiO_3$ (STO) as the substrate, thin YSZ/STO multilayers were found to exhibit colossal O ion conductivity, with enhancements of up to eight orders of magnitude near room temperature [59]. Given the 7% lattice mismatch, it is at first sight surprising that no mismatch dislocations are found at the interfaces (see Fig. 9).

The reason again lies in the response of the O sublattice, which essentially melts under the combined influence of the lattice mismatch strain and the incompatibility of the O sublattices between the fluorite structure of YSZ and the perovskite structure of STO, which makes it impossible to maintain continuity of the O sublattice across the interface. Computer simulations show that, under the influence of lattice strain alone, the O sublattice forms a zigzagged phase at 1000 K and becomes increasingly disordered at higher temperatures, as shown in Fig. 10. With the superlattice, however, the O sublattice was disordered even down to room temperature [60].

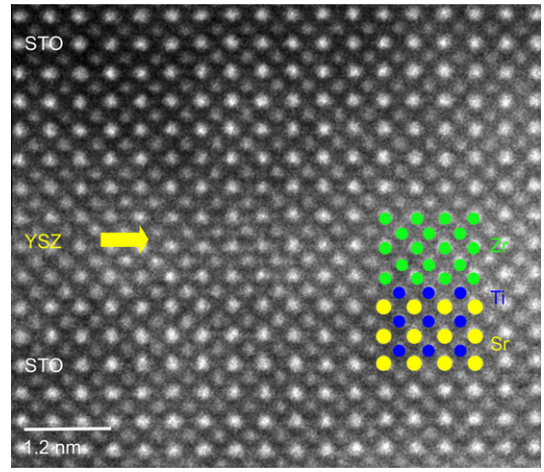

Fig. 9. Z-contrast image of a two unit cell layer of YSZ between STO layers (yellow arrow), with a superimposed structure model of the cation lattice. The interface termination was determined from EELS. Adapted from Ref. [59]. The white arrow indicates the growth direction. (For interpretation of the references to colour in this figure legend, the reader is referred to the web version of this article.)

Recently, the O sublattice was imaged directly by EELS imaging at the O K edge, and although the O sublattice was clearly resolved in the STO, in the YSZ layer it was seen to indeed be completely disordered [61].

7. Summary

Misfit accommodation in oxides is significantly more diverse than in the more usual semiconductor materials due to the propensity of oxides to tolerate a large number of cation and/or anion vacancies, and because of the subtle structural variations that influence the local orbital hybridization and hence the electronic and magnetic properties. The ability to understand and control these diverse misfit accommodation mechanisms is the key to understanding

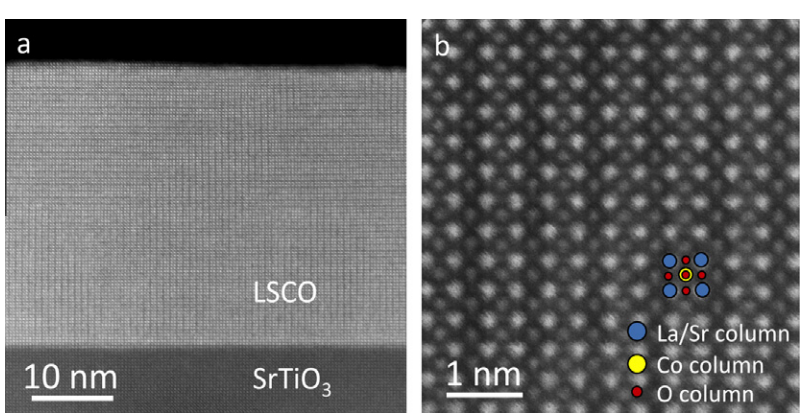

Fig. 8. Z-contrast images of a LSCO thin film: (a) low magnification, showing vertical and horizontal striped domains; (b) higher magnification, showing vertical dark stripes marking the vacancy containing Co planes. Images recorded on a Nion UltraSTEM100 at 100 kV.

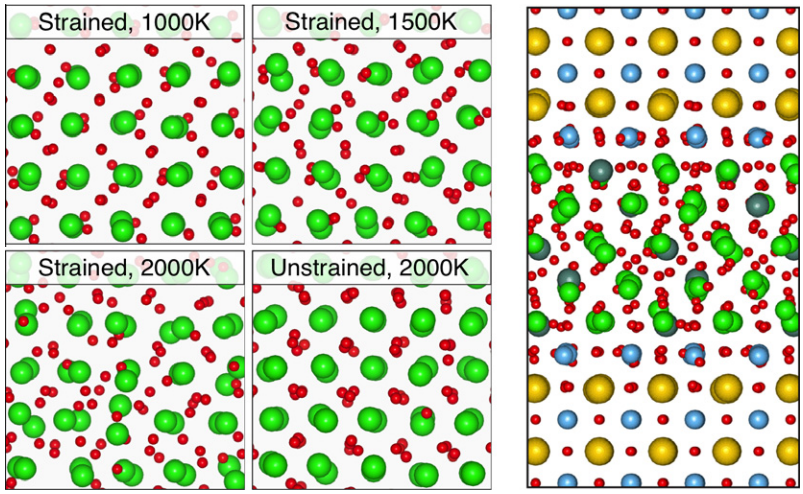

Fig. 10. (Left) Quantum mechanical simulated annealing at various temperatures. The 7% expansive strain is in the direction of the plane of the page. The zigzag ordering of the strained O sublattice shown at 1000 K persists down to 0 K, but begins to break down at higher temperatures. At 2000 K and above the O positions appear random, in contrast to the unstrained material, in which most O atoms simply oscillate about the cubic-fluorite positions. (Right) Structure of a 1 nm YSZ layer sandwiched between STO layers. O atoms are shown as small red spheres, Zr atoms in green, Sr in yellow, Ti in blue and Y in gray. Adapted from Ref. [60]. (For interpretation of the references to colour in this figure legend, the reader is referred to the web version of this article.)

and utilizing the intriguing interfacial phenomena in oxides.

Acknowledgements

This work was supported by the U.S. Department of Energy, Office of Basic Energy Sciences, Materials Sciences and Engineering Division (S.J.P., M.F.C., M.V., A.Y.B.), by a European Research Council Starting Investigator Award, Grant #239739 STEMOX (J.G.) and by the National Science Foundation (J.N., H.Z.).

References

[1] Chakhalian J, Freeland JW, Srajer G, Strempfer J, Khaliullin G, Cezar JC, et al. Nat Phys 2006;2:244.
[2] Reyren N, Thiel S, Caviglia AD, Kourkoutis LF, Hammerl G, Richter C, et al. Science 2007;317:1196.
[3] Okamoto S, Millis AJ. Nature 2004;428:630.
[4] Ohtomo A, Hwang HY. Nature 2004;427:423.
[5] Brinkman A, Huijben M, Van Zalk M, Huijben J, Zeitler U, Maan JC, et al. Nat Mater 2007;6:493.
[6] Chakhalian J, Freeland JW, Habermeier HU, Cristiani G, Khaliullin G, van Veenendaal M, et al. Science 2007;318:1114.
[7] Ichimuraa M, Narayan J. Philos Mag A 1995;72:281.
[8] Siddhartha M, Tsung-Han Y, Gupta P, Prater JT, Narayan J. Acta Materialia 2011;59:2526.
[9] Adler SB. J Am Ceram Soc 2001;84:2117.
[10] Crewe AV. Science 1983;221:325.
[11] Pennycook SJ, Jesson DE. Phys Rev Lett 1990;64:938.
[12] Pennycook SJ, Jesson DE. Ultramicroscopy 1991;37:14.
[13] Krivanek OL, Chisholm MF, Nicolosi V, Pennycook TJ, Corbin GJ, Dellby N, et al. Nature 2010;464:571.
[14] Borisevich AY, Chang HJ, Huijben M, Oxley MP, Okamoto S, Niranjan MK, et al. Phys Rev Lett 2010;105:087204.
[15] Pennycook SJ, Varela M, Lupini AR, Oxley MP, Chisholm MF. J Electron Microsc 2009;58:87.
[16] Varela M, Gazquez J, Pennycook SJ. MRS Bull 2012;37:29.
[17] Pennycook SJ, Nellist PD, editors. Scanning transmission electron microscopy: imaging and analysis. New York: Springer; 2011.
[18] Pennycook SJ, Varela M. J Electron Microsc 2011;60(Suppl. 1):S213.
[19] Duscher G, Pennycook SJ, Browning ND, Rupangudi R, Takoudis C, Gao HJ, et al. Structure, composition and strain profiling of Si/SiO_2 interfaces. Characterization and metrology for ULSI technology. Gaithersburg, MA: American Institute of Physics; 1998.
[20] Perovic DD, Rossouw CJ, Howie A. Ultramicroscopy 1993;52:353.
[21] Yu ZH, Muller DA, Silcox J. J Appl Phys 2004;95:3362.
[22] Xin Y, James EM, Arslan I, Sivananthan S, Browning ND, Pennycook SJ, et al. Appl Phys Lett 2000;76:466.
[23] Xin Y, James EM, Browning ND, Pennycook SJ. J Electron Microsc 2000;49:231.
[24] Xin Y, Pennycook SJ, Browning ND, Nellist PD, Sivananthan S, Omnes F, et al. Appl Phys Lett 1998;72:2680.
[25] Narayan J, Larson BC. J Appl Phys 2003;93:278.
[26] Chauveau JM, Laügt M, Venneguès P, Teisseire M, Lo B, Deparis C, et al. Semicond Sci Technol 2008;23:035005.
[27] Park S-H, Ahn D. Appl Phys Lett 2005;87:253509.
[28] Waltereit P, Brandt O, Trampert A, Grahn HT, Menniger J, Ramsteiner M, et al. Nature 2000;406:865.
[29] Zhang BP, Liu BL, Yu JZ, Wang QM, Liu CY, Liu YC, et al. Appl Phys Lett 2007;90:132113.
[30] Chauveau JM, Venneguès P, Lauegt M, Deparis C, Zuniga-Perez J, Morhain C. J Appl Phys 2008:104.
[31] Pant P, Budai JD, Aggarwal R, Narayan RJ, Narayan J. Acta Mater 2009;57:4426.
[32] Pant P, Budai JD, Narayan J. Acta Mater 2010;58:1097.
[33] Pennycook SJ, Jesson DE. Acta Metall Mater 1992;40:S149.
[34] Pennycook SJ, Chisholm MF, Jesson DE, Feenstra R, Zhu S, Zheng XY, et al. Physica C 1992;202:1.
[35] Pennycook SJ, Chisholm MF, Jesson DE, Norton DP, Lowndes DH, Feenstra R, et al. Phys Rev Lett 1991;67:765.
[36] Matthews JW, Blakeslee AE. J Cryst Growth 1974;27:118.
[37] Zhou H, Chisholm MF, Pant P, Chang HJ, Gazquez J, Pennycook SJ, et al. Appl Phys Lett 2010;97:121914.
[38] Kim M, Duscher G, Browning ND, Sohlberg K, Pantelides ST, Pennycook SJ. Phys Rev Lett 2001;86:4056.
[39] Klie RF, Buban JP, Varela M, Franceschetti A, Jooss C, Zhu Y, et al. Nature 2005;435:475.
[40] Voogt FC, Fujii T, Smulders PJM, Niesen L, James MA, Hibma T. Phys Rev B 1999;60:11193.
[41] Vaz CAF, Henrich VE, Ahn CH, Altman EI. J Cryst Growth 2009;311:2648.

[42] Graboy IE, Bosak AA, Gorbenko OY, Kaul AR, Dubourdieu C, Sénateur JP, et al. Chem Mater 2003;15:2632.
[43] Nag J, Haglund Jr RF. J Phys Condens Matter 2008;20:264016.
[44] Zhou H, Chisholm MF, Yang TH, Pennycook SJ, Narayan J. J Appl Phys 2011;110:073515.
[45] Gupta A, Narayan J, Dutta T. Appl Phys Lett 2010;97:151912.
[46] Hébert C, Willinger M, Su DS, Pongratz P, Schattschneider P, Schlögl R. Eur Phys J B – Condens Matter Complex Syst 2002;28:407.
[47] Jia CL, Lentzen M, Urban K. Science 2003;299:870.
[48] Pennycook SJ, Chisholm MF, Lupini AR, Varela M, Borisevich AY, Oxley MP, et al. Philos Trans Roy Soc A 2009;367:3709.
[49] Jia CL, Mi SB, Faley M, Poppe U, Schubert J, Urban K. Phys Rev B 2009;79:081405.
[50] Borisevich A, Ovchinnikov OS, Chang HJ, Oxley MP, Yu P, Seidel J, et al. ACS Nano 2010;4:6071.
[51] He J, Borisevich A, Kalinin SV, Pennycook SJ, Pantelides ST. Phys Rev Lett 2010;105:227203.
[52] Rondinelli JM, May SJ, Freeland JW. MRS Bull 2012;37:261.
[53] Rondinelli JM, Spaldin NA. Phys Rev B 2010;82:113402.
[54] Ito Y, Klie RF, Browning NS. J Am Ceram Soc 2002;85:969.
[55] Klenov DO, Donner W, Foran B, Stemmer S. Appl Phys Lett 2003;82:3427.
[56] Klie RF, Ito Y, Stemmer S, Browning NS. Ultramicroscopy 2001;86:289.
[57] Torija MA, Sharma M, Fitzsimmons MR, Varela M, Leighton C. J Appl Phys 2008;104:023901.
[58] Gazquez J, Luo WD, Oxley MP, Prange M, Torija MA, Sharma M, et al. Nano Lett 2011;11:973.
[59] Garcia-Barriocanal J, Rivera-Calzada A, Varela M, Sefrioui Z, Iborra E, Leon C, et al. Science 2008;321:676.
[60] Pennycook TJ, Beck MJ, Varga K, Varela M, Pennycook SJ, Pantelides ST. Phys Rev Lett 2010;104:115901.
[61] Pennycook TJ, Oxley MP, Garcia-Barriocanal J, Bruno FY, Leon C, Santamaria J, et al. Eur Phys J Appl Phys 2011;54:33507.